Predicting Atom-Level Models of Layered-Spinel Heterostructured Li-Mn-O Nanoparticles

R. S. Ledwaba[a], D. C. Sayle[b] and P. E. Ngoepe[a]

[a]Materials Modelling Centre, University of Limpopo, Private Bag X1106, Sovenga,0727, SA

[b]School of Physical Sciences, University of Kent, Canterbury, CT2 7NZ, UK.

ABSTRACT: Li-Mn-O heterostructured composite nanomaterials show promise as potential electrodes in energy storage devices. However, the structures of these materials are complex, which hinders understanding of their operation and future exploitation. Here, we capture such complexity, within atom-level models, by using simulated amorphization and recrystallization method on $LiMn_2O_4$. Analysis of the resulting Li-Mn-O nanoparticle models reveal that they comprise domains of defect-rich spinel, Mn_3O_4, layered Li_2MnO_3 and lithium-rich spinel $Li_{1+x}Mn_{2-x}O_4$ phases, which emanate from high temperature structural transformations. In addition, we observe grain-boundaries and intrinsic defects within the model structures. The discharge process was modelled by inserting surplus lithium atoms into the nanoparticles. This resulted in a decrease of both the Mn_3O_4 phase and the layered Li_2MnO_3-type structure concentration and the retention of the spinel $Li_{1+x}Mn_{2-x}O_4$ phases. Such models will help experiments unravel the hierarchical structural complexity of these composite materials. We also find that microstructural features, such as microtwinning and intrinsic dopants (vacancies, substitutionals and interstitials) result in a network of Li transport pathways, enabling Li mobility in all three spatial directions.

Introduction

The current application scope of LIBs has been expanded from consumer devices such as laptops and phones to transportation applications including electric vehicles (EVs) [1]. NMC is among the best cathode materials for the electrification of automobile vehicles given its advantages in high capacity, electrochemical stability, and cost effectiveness. [2-3], and much progress has been made in enhancing its performance, especially the nickel rich NMCs [4]. Although it is estimated that nickel has sufficient supply, the extent of deploying electro-mobility in the future could lead to its shortages [5]. Consequently, for long term sustainability of EVs on roads it is important to consider cathodes that use more abundant materials, such as manganese. Consideration of LMO cathodes means a compromise on energy density but a pronounced gain in rate capability, better low temperature performance, cost and high round energy efficiency per cycle [6].

It has been further reported that $LiMn_2O_4$ achieves an excellent cycle performance by blending with $LiMO_2$ (M: Mn, Co, Ni etc.) [7-10] which has been recently embedded in commercialized EVs. An understanding of the electrochemical behaviour of $LiMn_2O_4$ could be also extended to the analysis of related high-voltage electrodes such as $LiNi_{0.5}Mn_{1.5}O_4$.[11,12]. In Li-rich NMCs, the composite layered spinel structures have played a significant role in enhancing capacity and suppressing voltage fade [13]. Nanoparticle-aggregated microspheres (primary and secondary) of Li-rich “layered (R-3m)–layered (C2/m)–spinel (Fd-3m)” materials showed simultaneously great reversible capacity (302 $mAh \cdot g^{-1}$ at 0.2 C), higher initial Coulombic efficiency and superior rate capability, when compared to pure layered Li-rich material [14-17]. In addition, the increase in the cyclability and rate capability were attributed to the flexibility of smaller particles and their exposed large surface areas allowed faster charge/discharge because of the shortened electron and lithium ion diffusion distances [18,19]. Also all Mn – NMC (Johnson and Thackeray 2005) [20] .

The presence of the spinel and layered structures in NMC cathodes, is inherent/typical of the spinel $LiMn_2O_4$, owing to its varied high temperature behaviour. The study by Thackeray al [21, 22] revealed that on heating this compound from ambient

temperature, a (rock-salt) Li_2MnO_3 phase is formed at approximately 800K, which is followed by a high temperature spinel Mn_3O_4 phase that emerges around 1120°C (1393.15 K). The study has also shown that the spinel phase comprises a high concentration of manganese occupying tetrahedral sites and attributed this to the loss of oxygen and lithium (as Li_2O) [23].

In principle, the spinel-Mn_2O_4 framework can deliver a capacity of ~297 $mAhg^{-1}$ when a Li^+ ion is inserted/extracted into/from each of the 8a tetrahedral and 16c octahedral sites. However, the strong Jahn−Teller distortion of MnO_6 octahedra that occurs due to Mn^{3+} formation, leads to a partly reversible phase transition that is associated with the 2.7 V plateau. An increase in the axial ratio c/a of the unit cell from 1.0 in the cubic phase to 1.6 in the distorted tetragonal phase is induced by the lithiation of $Li_{1+\delta}Mn_2O_4$ ($0 \leq \delta \leq 1$). Such anisotropic strain causes fracture of large particles and thus internal contact loss upon cycling [25-27]. Accordingly, NPD and first principles calculations proposed a comprehensive understanding on the reaction mechanisms involving the solid-solution regions within both cubic and tetragonal symmetries in addition to the two-phase transition between them [28].

Simulated amorphisation and recrystallization method, based on molecular dynamics methods, has been successfully employed to ‘synthesis’ various nano-architectures (nano- spheres, sheets, porous) of the binary CeO_2 [29] and Li-ion battery electrodes such as MnO_2 [30,31] and TiO_2 [32]. In addition, the method yielded heterostructured or composite compounds with ramsdellite-pyrolusite and rutile-brookite polymorphs for MnO_2 and TiO_2 respectively. A model ternary Li_2MnO_3 nanosphere, has also been synthesised using this approach [33]. The A+R method allows for ‘spontaneous’ nucleation and growth of crystals with microstructural features, such as grain-boundaries, dislocations and point defects occurs exothermically. Microstructures are consistent with those observed from the high resolution transmission microscope. In-depth understanding of such microstructural features and active sites of ions can aid in the design and modification of high energy density electrode materials [34, 35],

In the present study, we use the simulated amorphization and recrystallization method to generate atom-level models of $Li_xMn_2O_4$ ($1 \leq x \leq < 2$) nanoparticles, often referred to as primary particles. This will be followed by simulation of the charge/discharge

process, conducted by subsequently inserting lithiums into the nanoparticles whilst closely monitoring the effect of lithiation on the structural integrity of the host electrode material. The conditions for simulation will be guided by high temperature molecular dynamics simulation data reported in our previous work [26]. Proper harvesting and analysis of the microstructures for nanoparticles with different lithium concentrations can help to elevate understanding of the cubic to tetragonal spinel transition so crucial for the performance of this cathode.

New References:

1. F. T. Wagner, B. Lakshmanan and M. F. Mathias, J. Phys. Chem. Lett., 2010, 1, 2204.

2. D. Andre, S.-J. Kim, P. Lamp, S. F. Lux, F. Maglia, O. Paschos, and B. Stiaszny, J. Mater. Chem. A, **3**, 6709 (2015).

3. K. G. Gallagher, S. Goebel, T. Greszler, M. Mathias, W. Oelerich, D. Eroglu, and V. Srinivasan, Energy Environ. Sci., **7**, 1555 (2014).

4. R. Jung, M. Metzger, F. Maglia, C. Stinner, and H. A. Gasteiger,J. Electrochem.Soc.,164, A1361 (2017).

5. To be added

6. M. M. Thackeray, C. S. Johnson, J. T. Vaughey, N. Li, and S. A. Hackney, Journal of Materials Chemistry, **15**, 2257 (2005).

7. T. Numata, C. Amemiya, T. Kumeuchi, M. Shirakata and M. Yonezawa, J. Power Sources, 2001, 97–98, 358.

8. S. T. Myung, M. H. Cho, H. T. Hong, T. H. Kang and C. S. Kim, J. Power Sources, 2005, 146, 222.

9. J. Belt, V. Utgikar and I. Bloom, J. Power Sources, 2011, 196, 10213.

10. Z. Mao, M. Farkhondeh, M. Pritzker, M. Fowler and Z. Chen, "Charge/Discharge Asymmetry in Blended Lithium-Ion Electrodes", *J. Electrochem. Soc.*, 164, A39-47 (2017).

11. R. Santanam and B. Rambabu, J. Power Sources, 2010, 195, 5442.

12. A. Sakunthalaa, M. V. Reddya, S. Selvasekarapandian, B. V. R. Chowdaria and P. Christopher Selvin, Electrochim. Acta, 2010, 55, 4441.

13. Long B. R., Croy J. R., Park J. S., Wen J., Miller D. J. and Thackeray M. M., "Advances In Stabilizing 'Layered-Layered'xLi_2MnO_3·(1-X) $LiMO_2$ (M= Mn, Ni, Co) Electrodes With A Spinel Component," *Journal Of The Electrochemical Society,* **161**, A2160-A2167, 2014

14. Deng Y. P., Yin Z. W., Wu Z. G., Zhang S. J., Fu F., Zhang T., Li J. T., Huang L. and Sun S.G., "Layered/Spinel Heterostructured and Hierarchical Micro/Nanostructured Li-Rich Cathode Materials With Enhanced Electrochemical Properties For Li-Ion Batteries," *ACS Applied Materials & Interfaces,* **9**, 21065-21070, 2017

15. Luo D., Li G., Fu C., Zheng J., Fan J., Li Q. and Li L., "A New Spinel-Layered Li-Rich Microsphere As A High-Rate Cathode Material For Li-Ion Batteries," *Advanced Energy Materials,* **4**, 1400062-1400062, 2014

16. Deng Y. P., Fu F., Wu Z. G., Yin Z. W., Zhang T., Li J. T., Huang L. And Sun S. G., "Layered/Spinel Heterostructured Li-Rich Materials Synthesized By A One-Step Solvothermal Strategy With Enhanced Electrochemical Performance For Li-Ion Batteries," *Journal of Materials Chemistry A,* **4**, 257-263, 2016

17. Wu F., Li N., Su Y., Shou H., Bao L., Yang W., Zhang L., An R. and Chen S., *Advanced Materials,* **25**, 3722-3726, 2013.

18. Huang H., Vincent C. A. and Bruce P. G, "Correlating Capacity Loss of Stoichiometric and Nonstoichiometric Lithium Manganese Oxide Spinel Electrodes With Their Structural Integrity," *Journal of the Electrochemical Society,* **146**, 3649-3654, 1999

19. Xia H., Luob Z. and Xieb J., "Nanostructured $LiMn_2O_4$ and Their Composites as High-Performance Cathodes for Lithium-Ion Batteries," *Progress In Natural Science: Materials International,* **22**, 572-584, 2012

20. Johnson C. S., Li N., Vaughey J. T. , Hackney S. A. and Thackeray M. M., "Lithium–Manganese Oxide Electrodes with Layered–Spinel Composite Structures $xLi_2MnO_3\cdot(1-x)\ Li_{1+y}Mn_{2-y}O_4$ ($0< x< 1$, $0\leqslant y\leqslant 0.33$) for Lithium Batteries," *Electrochemistry Communications,* **7**, 528-536, 2005

21. Thackeray M. M., David W. I. F., Bruce P. G. and Goodenough J. B., "Lithium Insertion Into Manganese Spinels," *Materials Research Bulletin,* **18**, 461-472, 1983.

22. Thackeray M. M., Mansuetto M. F., Dees D. W. and Vissers D. R., "The Thermal Stability of Lithium-Manganese-Oxide Spinel Phases," *Materials Research Bulletin,* **31**, 133-140, 1996.

23. Komaba S., Sasaki T. and Kumagai N., "Preparation And Electrochemical Performance of Composite Oxide of Alpha Manganese Dioxide and Li–Mn–O Spinel," *Electrochimica Acta,* **50**, 2297-2305, 2005.

24. Looking for a relevant reference, if possible.

25. Tarascon, J. M.; Guyomard, D. Li Metal-Free Rechargeable Batteries Based on Li1+xMn2O4 Cathodes (0≤x≤1) and Carbon Anodes. J. Electrochem. Soc. 1991, 138, 2864−2868.

26. Paulsen, J. M.; Thomas, C. L.; Dahn, J. R. Layered Li-Mn-oxide with the O2 structure: A cathode material for Li-ion cells which does not convert to spinel. J. Electrochem. Soc. 1999, 146, 3560−3565.

27. Van der Ven, A.; Marianetti, C.; Morgan, D.; Ceder, G. Phase transformations and volume changes in spinel Li_xMn2O4. Solid State Ionics 2000, 135, 21−32.

28. B. Song, G.M. Veith, J. Park, M. Yoon, P.S. Whitfield, M.J. Kirkham, J. Liu and A. Huq, Metastable $Li_{1+\delta}Mn_2O_4$ ($0 \leq \delta \leq 1$) spinel phases revealed by in operando neutron diffraction and first-principles calculations Chem. Mater. (2019), **31**,1124-134.

29. Sayle T.X., Parker S.C., Sayle D.C., “Shape of CeO_2 nanoparticles using simulated amorphisation and recrystallisation", Chem. Commun., 7, 2438-9, 2004. – Sayle 2019.

30. Sayle T. X. T., Maphanga R. R., Ngoepe P. E. And Sayle D. C., "Predicting The Electrochemical Properties of MnO_2 Nanomaterials Used In Rechargeable Li Batteries: Simulating Nanostructure at the Atomistic Level," *Journal of the American Chemical Society,* **131**, 6161-6173, 2009

31. T.X.T. Sayle, K. Kgatwane, P.E. Ngoepe and D.C. Sayle, ‘Breathing-Crystals’ - The origin of electrochemical activity of mesoporous Li-MnO_2, Journal of Materials Chemistry A, (2016), **4**, 6456-6464,

32. Matshaba M. G., Sayle D. C., Sayle T. X. and Ngoepe P. E., "Structure of Surface Entrance Sites For Li Intercalation Into TiO_2 Nanoparticles, Nanosheets and Mesoporous Architectures With Application for Li-Ion Batteries," *The Journal of Physical Chemistry C,* **120**, 14001–14008, 2016

33. Sayle T. X. T., Caddeo F., Monama N. O., Kgatwane K. M., Ngoepe P. E. and Sayle D. C., "Origin Of Electrochemical Activity In Nano-Li_2MnO_3; Stabilization via a 'Point Defect Scaffold'," *Nanoscale,* **7**, 1167-1180, 2015

34. Maphanga R. R., Sayle T. X. T., Ngoepe P. E. and Sayle D. C., "Amorphization and Recrystallization Study of Lithium Insertion Into Manganese Dioxide," *Physical Chemistry Chemical Physics,* **13**, 1307-1313, 2011.

35. Liu C., Neale Z. G. and Cao G., "Understanding Electrochemical Potentials of Cathode Materials In Rechargeable Batteries," *Materials Today,* **19**, 109-123, 2016.

2. Method

In this section we discuss briefly, the potential models used to describe the interactions between Li–Mn-O ions, the codes used to perform the dynamical simulations, the construction of atomistic models, their amorphization and recrystallization as well as the discharge process.

Potential models: Simulations in this work are based on interatomic potentials that were previously generated and reported for the Born model of the ionic solids, in which the Mn^{4+}, Mn^{3+}, Li^{+} and O^{2-} ions interact via long-range Coulombic interactions coupled with short-range parameterized interactions [24].

Simulation code: The DL_POLY [27] code was used to perform all the molecular dynamics (MD) simulations. This code utilizes three-dimensional periodic boundary conditions to represent the model infinitely in space. All simulations were performed within the NVE and NVT ensembles, for amorphization and recrystallization, respectively.

Generating atomistic models: The nanoparticle was generated by cleaving a sphere with desired radius from the parent bulk. Stoichiometry was assured by removing either Mn/O/Li atoms from the outer surface to facilitate charge neutrality resulting in a nanoparticle with 26 642 atoms (8nm in diameter). A spinel structured crystalline seed in the form of a cube (morphology) was fixed at the centre of the nanoparticle during amorphization.

Amorphization and recrystallization: The nanoparticle was amorphized at 1700K, while enclosed in a 100 Å box, which limits interaction with neighbouring nanoparticles and has dimensions sufficiently large in order for it not to interact with its images. The system was then allowed to recrystallize, during which time the ions had sufficiently

high mobilities to allow them to move into low-energy configurations within the timescales (typically nanoseconds) accessible to the simulation allowing evolution of microstructural features, such as: grain-boundaries, dislocations, point defects, as observed experimentally [28].

Lithium intercalation: Lithium atoms were introduced into the spinel nanoparticle, specifically, four models were generated: $Li_{1.25}Mn_2O_4$, $Li_{1.5}Mn_2O_4$, $Li_{1.75}Mn_2O_4$ and $Li_{2.0}Mn_2O_4$ i.e. three nanospheres with different concentrations were obtained containing 4758, 5709, 6661 and 7360 lithium atoms, respectively. The program uploaded the insertion sites from the structure file, randomly selected a tunnel site and inserted a lithium ion at its vacant co-ordinates. Charge neutrality was maintained by reducing an Mn^{4+} ion, closest to the (inserted) lithium cation, to Mn^{3+}. This process was repeated for all the lithium ions inserted in the structure.

3. Results

Recrystallisation: MD simulation, performed at 1700 K for 5 ns, led to the complete crystallization of the nanoparticle - nucleated by the crystalline seed, at the centre of the nanoparticle. A low energy structure was achieved by reducing the temperature to 1 K; the MD acts as a pseudo energy minimization. The initial crystalline nanoparticle model, is shown in Figure 1 (a) with atoms occupying Wyckoff positions depicted in (b), followed by the amorphous system in (c) and SEM image of nanoparticle synthesized experimentally via the ultrasonic spray pyrolysis method(d) [28], the polycrystalline nanosphere obtained after recrystallization is shown in (e) with lithiums occupying 16c sites, in (f, g).

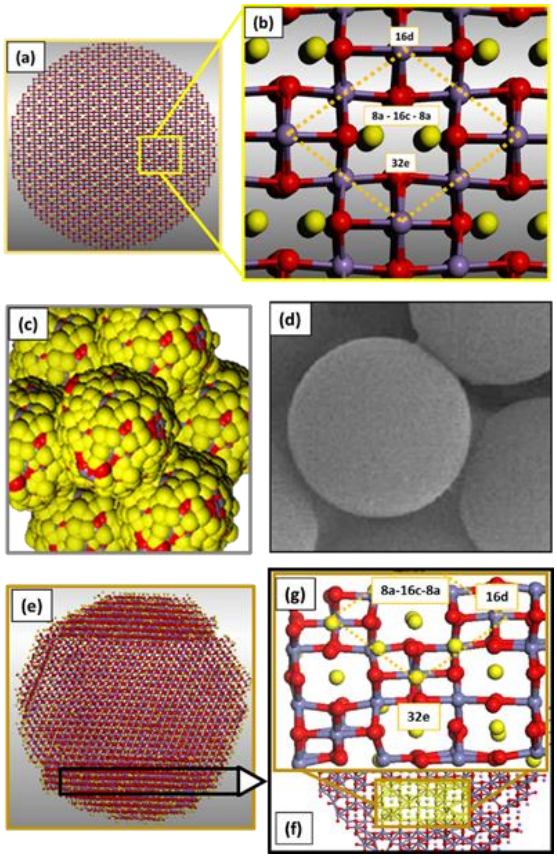

Figure 1: Spinel $LiMn_2O_4$ (a) crystalline nanosphere cleaved from the parent bulk, (b) atomic Li -Mn-O sites from crystalline model, (c) amorphous Li-Mn-O nanoparticles (d) SEM images of the $LiMn_2O_4$ nanoparticle [28], (e) recrystallized nanospheres of Li-Mn-O and (f, g) slice cut from recrystallized sphere depicting atomic Li-Mn-O sites.

Figure 2 illustrates the steps-by-step recrystallization of the Li-Mn-O nanoparticle. The initial amorphous Li-Mn-O structure is shown at time t= 0 ns. Crystallisation started around 0.3 ns, nucleated by the crystalline seed at the centre of the nanoparticle – and was complete after 0.6 ns. Crystallization was observed to propagate along different directions, resulting in the formation of a polycrystalline material with grain boundaries.

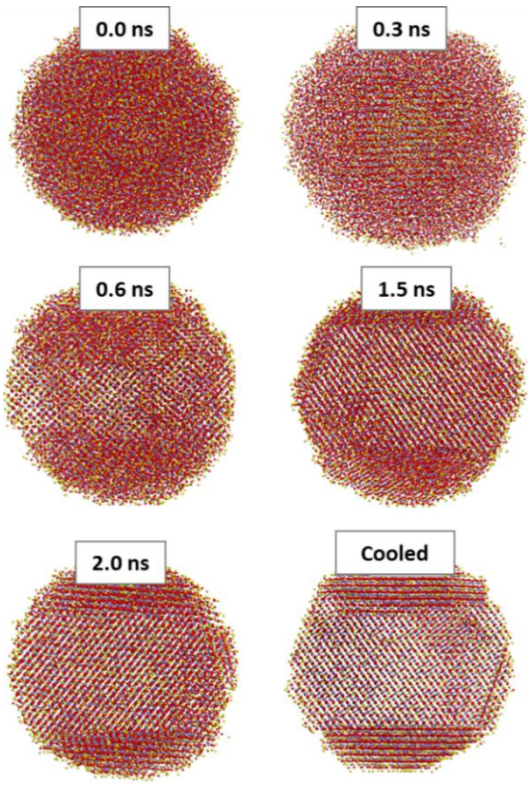

Figure 2: Atomistic structure of the Li-Mn-O nanoparticle with 26 642 atoms during crystallization at 0 ns, 0.3 ns, 0.6 ns, 1.5 ns, 3.0 ns and after cooling.

Amorphous RDFs: The radial distribution function (rdfs) plots for amorphized nanosphere are shown in figure 3 (a). They depict the first peak at ~1.95 Å for Mn-O, ~2.5 for O-O and ~3 Å for Mn-Mn, which represent the bond lengths between the relative atom species. These are followed by broader peaks beyond 5 Å radial distance, indicating that the nanosphere is in a disordered state and that the probability of locating the nearest neighbouring atom in relation to the reference atom is minimal.

Recrystallised RDFs: In figure 3 (b) below, there is an increase in peak quantity and sharpness of the rdfs. The peaks attributable to Mn-O, Mn-Mn and O-O interactions occur between 2 and 4 Å. Sharper peaks emanate beyond 4 Å, for Mn-O, Mn-Mn and O-O interactions, indicating long-range order and therefore confirming that the spinel nanosphere has recrystallized.

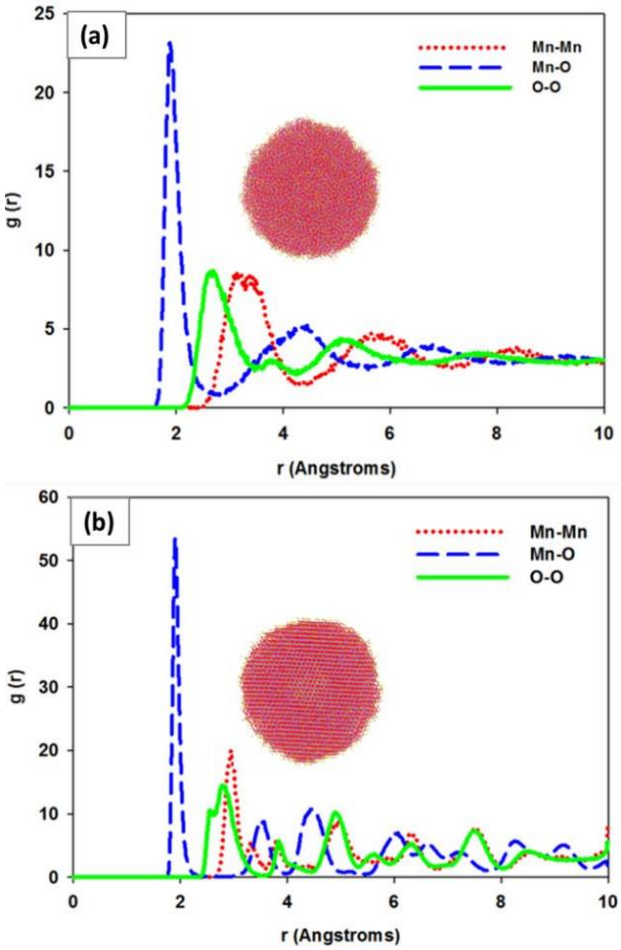

Figure 3: RDFs of the Li-Mn-O nanosphere (a) before crystallization and (b) after crystallization at 1700 K.

Cooled RDFs: The recrystallized structure was then cooled by performing MD simulations for: 500 ps at 1200 K, 250 ps at 800 K, 250 ps at 400 K and lastly 500 ps at 0 K. This helps remove thermal noise from the structure and makes characterisation easier. The total RDFs of the nanosphere at different temperatures are shown in figure 4. Lowering of temperature increases peak sharpness and this is particularly distinct in the enlarged portion, in (b) where narrowing of peaks at different temperatures is clearly depicted, implying that the system is more crystalline.

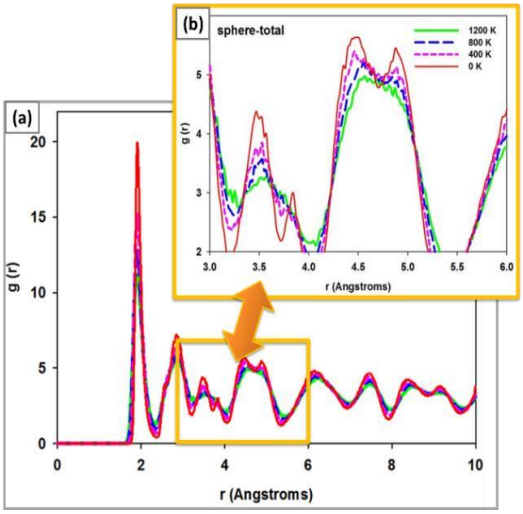

Figure 4: Total RDFs of the Li-Mn-O nanosphere at different temperatures (a) and its magnified portion in (b).

Characterization: In figure 5, a snapshot of the Li-Mn-O nanosphere is shown. A portion from this nanosphere is magnified in (b) to clearly show the occupancy of manganese (Mn) atoms on tetrahedral sites. Some atomic arrangements in this portion are similar to those of spinel Mn_3O_4. As such, the conventional unit cell of spinel Mn_3O_4 structure was captured in (c) and compared with a similar segment magnified from (b). The compatibility thereof suggested the presence of spinel Mn_3O_4 within the recrystallized Li-Mn-O nanosphere (a).

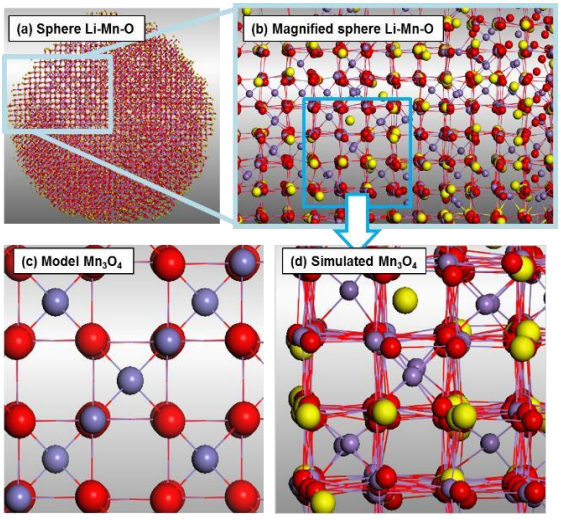

Figure 5: (a) Recrystallized Li-Mn-O nanosphere, (b) magnified portion of the nanosphere with tetrahedral Mn, (c) conventional unit cell of perfect spinel Mn_3O_4 showing structural arrangement and (d) magnified portion of (b) where an Mn_3O_4-type of arrangement is observed within the recrystallized Li-Mn-O nanosphere.

Detailed analysis was carried out by cutting through the nanosphere in the area enclosed with a white box in figure 6 (a). A snapshot of the slice is shown in (b), illustrating the atomic arrangement of Li, Mn and O atoms, which conform to a defective (layered) Li_2MnO_3 crystal structure. The model of perfect Li_2MnO_3 in (c) was compared with the magnified portion of (b) denoted as (d). Although the magnified portion in (d) is defective with vacancies and substitutions, the atomic arrangements comparable to those observed in (c).

Comparison between Li-Mn-O atomic arrangements calculated in this work and measured experimentally by Long et al [6], are shown in figure 7. The atomic arrangement is similar to that of $Li_4Mn_5O_{12}$ (lithium-rich phase of $Li_{1+x}Mn_{2-x}O_4$) in which lithium atoms occupy 16d positions. Conversely, in $LiMn_2O_4$ Mn atoms are located on these sites. This lithium-rich phase is advantageous because it suppresses Jahn-Teller distortions due to its oxidation state of Mn^{4+} [14] unlike $LiMn_2O_4$ which experiences domination of Mn^{3+} during redox reactions of the charge and discharge process. In addition to this phase, another slice showed the presence of Li_2MnO_3 within the nanosphere in (d). This layered structure accords with the HRTEM image of diffraction spots for layered Li_2MnO_3 characterized experimentally by Long et al in (e) [6].

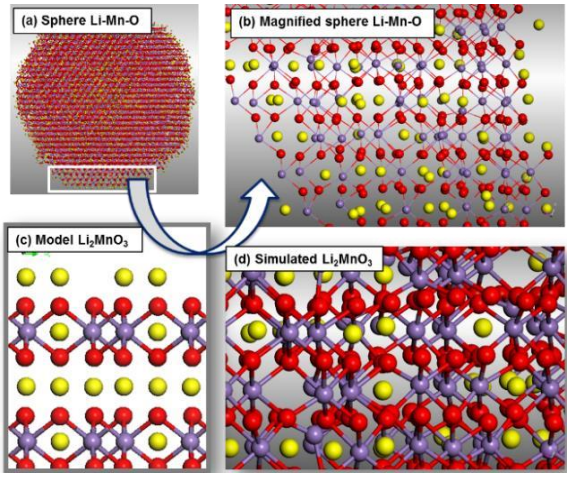

Figure 6: (a) Schematic representation of recrystallized spinel, (b) slice cut through the nanoparticle, (c) slice cut through a perfect bulk model of Li_2MnO_3 and (d) magnified portion of the slice in (b) showing the presence of Li_2MnO_3.

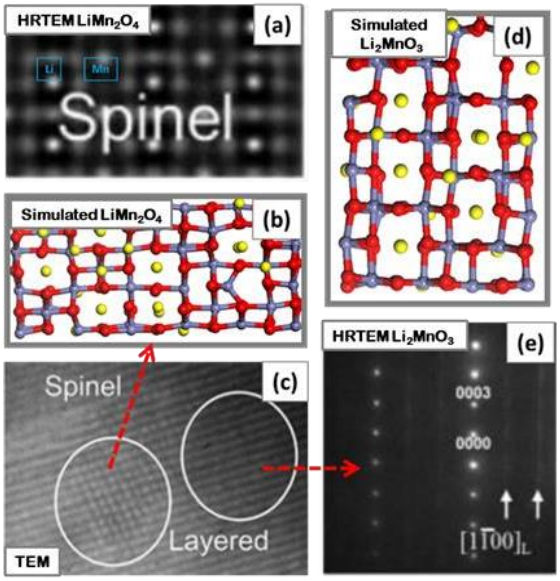

Figure 7: (a) HRTEM image of defective spinel $Li_4Mn_5O_{12}$ [6] (b) simulated spinel component (this work) in Li-Mn-O nanosphere, (c) Experimental co-existing spinel and layered composite [3], (d) simulated Li_2MnO_3 phase in Li-Mn-O nanosphere and (e) experimental diffraction spots of Li_2MnO_3 structure [6].

Discharge Process: Nanospheres with various lithium concentrations are illustrated by the snapshots in figure 8. The structures illustrate crystallization along different directions from $Li_{1.00}Mn_2O_4$ to $Li_{1.50}Mn_2O_4$. The $Li_{1.75}Mn_2O_4$ nanoparticle, exhibits extensive multiple grains, and it subsequently transforms into a single crystalline phase after full lithiation, at $Li_{2.0}Mn_2O_4$**.** The structural variations observed in snapshots correspond to changes in the voltage profile across the concentration range. In order to understand the effect of lithiation on the structural integrity of the host Li-Mn-O material, the nanospheres were characterised using graphical techniques, particularly for composition $Li_{1.75}Mn_2O_4$ and $Li_{2.00}Mn_2O_4$ as shown in figure 9 (1) and (2), respectively. In segment (1), a slice (b), depicting the co-existence of magnified layered (c) and spinel (e) components within the lithiated Li-Mn-O nanosphere, was cut through (a). The simulated layered component was compared to the atomic arrangement of perfect (bulk) Li_2MnO_3 in (d) and similarities were observed in terms of atomic arrangements. Furthermore, a larger portion on the same slice (e), conforms to the spinel crystal structure; a model of the perfect (bulk) spinel $Li_{1+x}Mn_2O_4$ unit cell is shown in (f). Segment 2 illustrates dominance of the spinel component on the microstructures cut across slices 1-3. This may imply that after transformation from

$Li_{1.75}Mn_2O_4$, predominance of spinel phase occurs unlike composites observed at lower Li concentrations

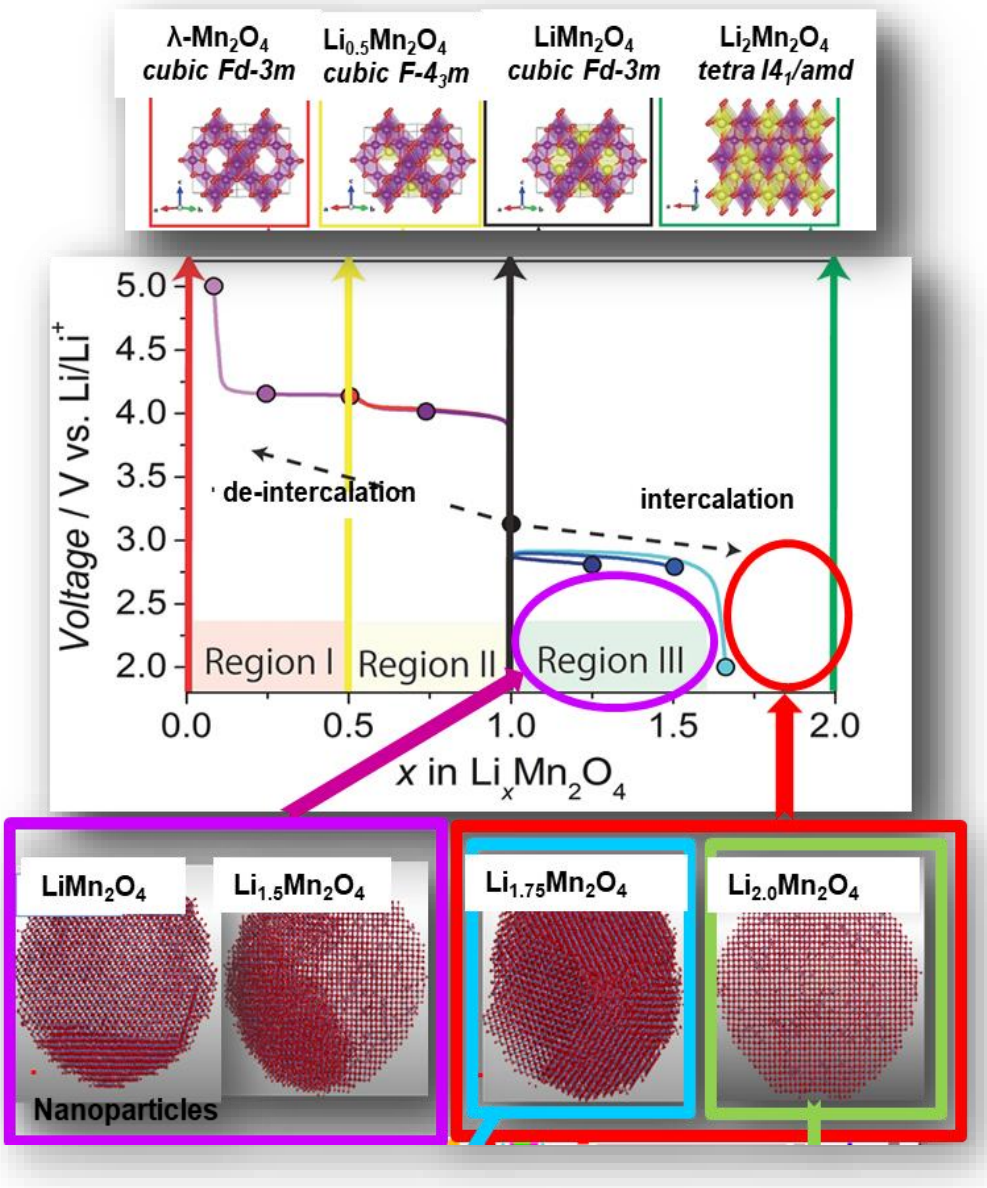

Figure 8: (i) Nanospherical $Li_xMn_2O_4$ with various lithium concentrations where: (a) $Li_{1.00}Mn_2O_4$, (b) $Li_{1.25}Mn_2O_4$, (c) $Li_{1.25}Mn_2O_4$, (d) $Li_{1.75}Mn_2O_4$ and (e) $Li_{2.00}Mn_2O_4$.

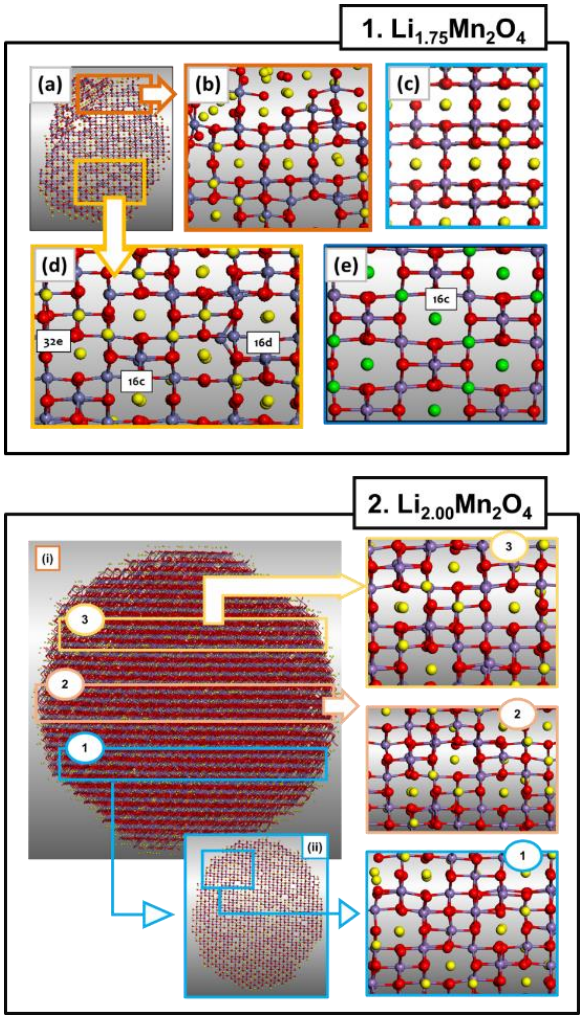

Figure 9: [1] (a) Slice cut through $Li_{1.75}Mn_2O_4$ nanosphere depicting (b) slight Li_2MnO_3–type arrangement, (c) model Li_2MnO_3, (d) spinel component in $Li_{1.75}Mn_2O_4$ and (e) model of spinel $Li_4Mn_5O_{12}$. (i) Recrystallized nanosphere of $Li_{2.00}Mn_2O_4$ cut across 3 segments illustrating predominance of spinel components in the microstructures.

Figure 10 demonstrates the intermediate phases identified during lithiation of $Li_{1.5}Mn_2O_4$ at atomistic level (i, iii) compared with similar findings from first-principles calculations (ii, iv) [29]. The Mn−O bond lengths from nanospherical $Li_{1.5}Mn_2O_4$, illustrate both $Mn^{3+}O_6$ and $Mn^{4+}O_6$ octahedra with characteristic features of the (a) cubic-$Li_{1.5}Mn_2O_4$ (b) and tetragonal-$Li_{1.5}Mn_2O_4$ intermediate phases. The bond length of $Mn^{3+}O_6$ along the c-axis follows the increase trend from by a factor of 0.08 in this work which with agrees well with the 0.07 factor observed in first principle calculations [29]. This implies similar observations of structural transitions in the spinel structure.

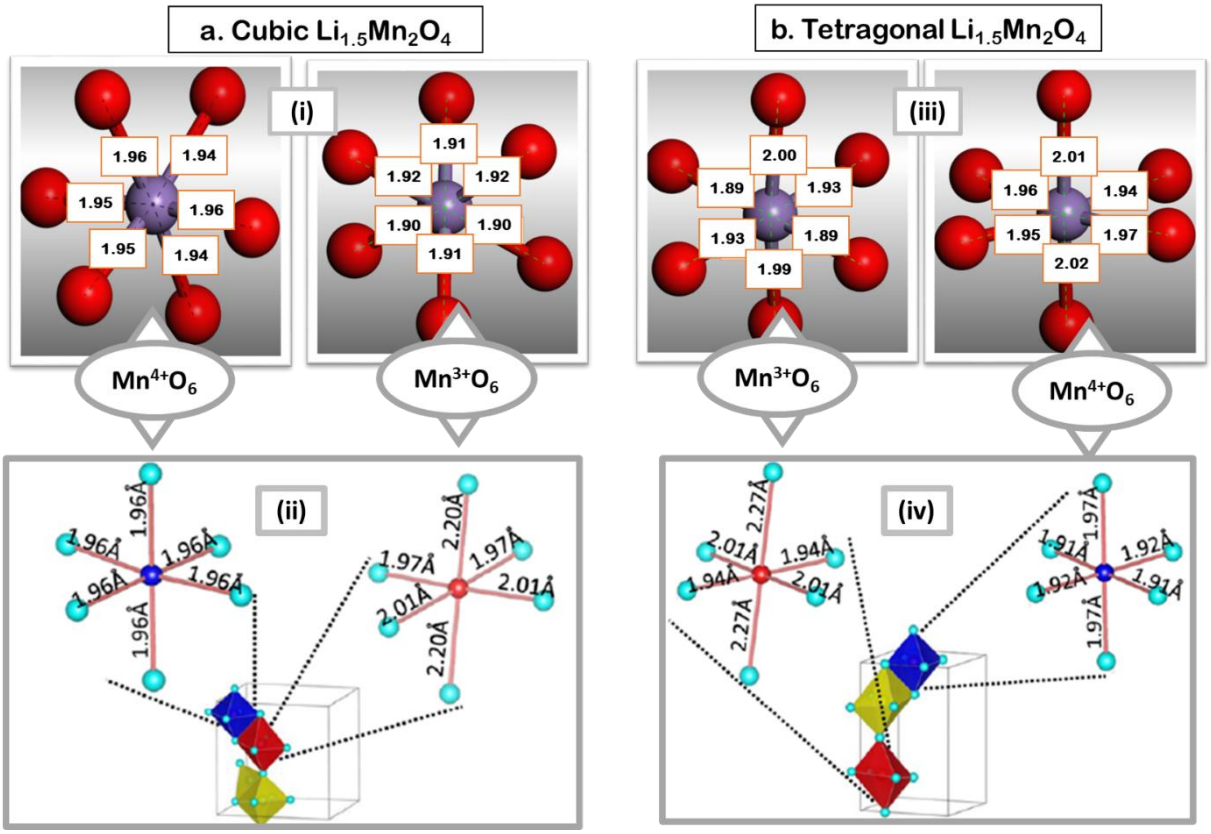

Figure 10: (a) The Mn−O bond lengths of $Mn^{3+}O_6$ and $Mn^{4+}O_6$ octahedra in the cubic-$Li_{1.5}Mn_2O_4$ calculated with (i) atomistic simulations and (ii) first principle calculations. (b) tetragonal-$Li_{1.5}Mn_2O_4$ based on (iii) atomistic simulations and (iv) first principle calculations.

Crystallographic Defects: In figure 11, the recrystallized nanoparticle is depicted in (a) and consists of ~10 nm scale similar to that shown by the TEM in (b). High resolution of simulated spinel $LiMn_2O_4$ is shown in magnification of (a) below, highlighting the polycrystallinity of the nanoparticle during synthesis as it was found in experiments and depicted in the high resolution TEM (b) below. The yellow boxes in magnifications of (a) and (b) represent the spinel tunnels on the nanomaterials. Further analysis was carried out by cutting a slice through the nanosphere and changing the atomic display into spheres as shown in figure 10. Snapshot (1) depicts grain boundaries denoted by pink dots. A segment from the middle of the slice was enlarged on the right of image (1) illustrating Li-Mn-O atomic arrangements and is shown using polyhedral rendering (2) and CPK (3) format. Point defects, such as substitution of Mn atoms by Li atoms at some atomic sites (green rectangle), were observed together

with Mn vacancies (green circles). Substitution of Mn by Li enables Li mobility within the material; possible pathways are indicated by the red arrows in (2). The CPK format in (3) helps to show that atoms within the system are well ordered despite the complex defect microstructure. The nanoparticle consists of grain boundaries as shown in (1) and the upper grain boundary region is indicated on the slice cut through the nanosphere in (4) by stick representation. Magnification of the grain boundary region in (4) is illustrated by a black oval on the right depicting atoms ordered along different directions at approximately 45 degrees angle.

The recrystallized nanosphere (6661 lithium atoms), with a structural composition of $Li_{1.75}Mn_2O_4$, is depicted in figure 12 (a). The sphere contains ordered patterns of Li, Mn and O atoms along different directions. A portion of this nanosphere was sliced along the white dotted lines and the slice is shown in (b) below. The same slice is presented in (c) for oxygen layers, with CPK representation to showing grain boundaries in regions labelled 1-6 and lastly a segment was magnified in (d), depicting several point defects such as interstitials (blue box) and vacancies (light orange box) that occur within the nanosphere. This indicates the presence of Frenkel defects in the $Li_{1.75}Mn_2O_4$ nanosphere system.

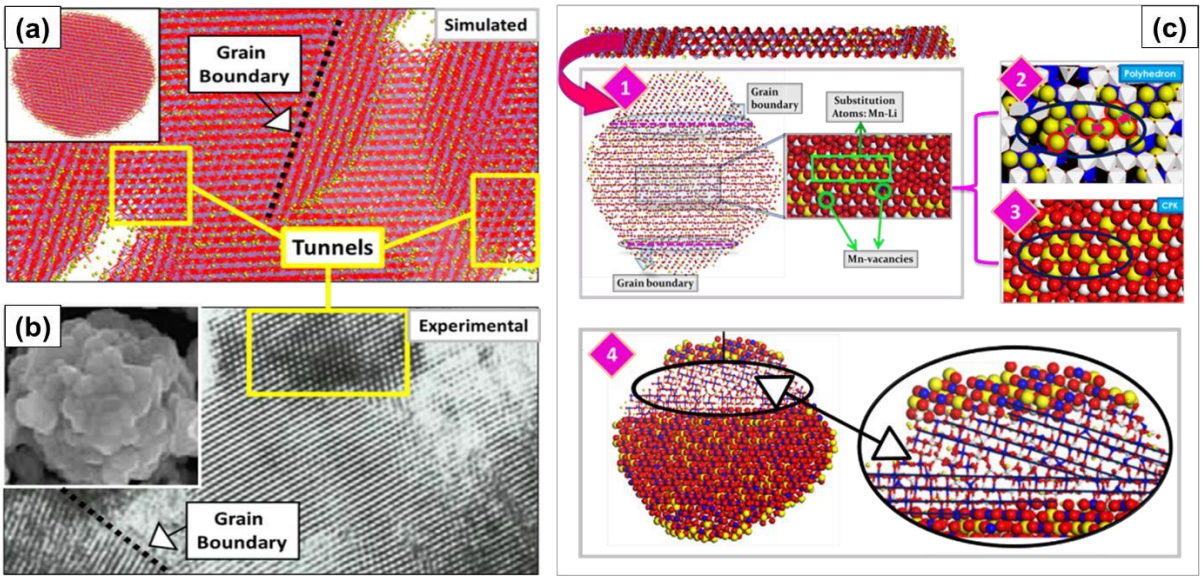

Figure 11: (a) Snapshot of recrystallized Li-Mn-O nanosphere (this work) with 26 642 atoms and its magnified resolution showing tunnels in yellow boxes and (b) TEM images of the $LiMn_2O_4$ nanoparticle with high resolution TEM image of the $LiMn_2O_4$

powder [19]. (c) (1) Slice cut through the Li-Mn-O nanosphere with 26 642 atoms revealing crystallographic defects such as (2, 3) point defects and (4) grain-boundary structure that has evolved during recrystallization and enlarged segment of the grain boundary (black oval).

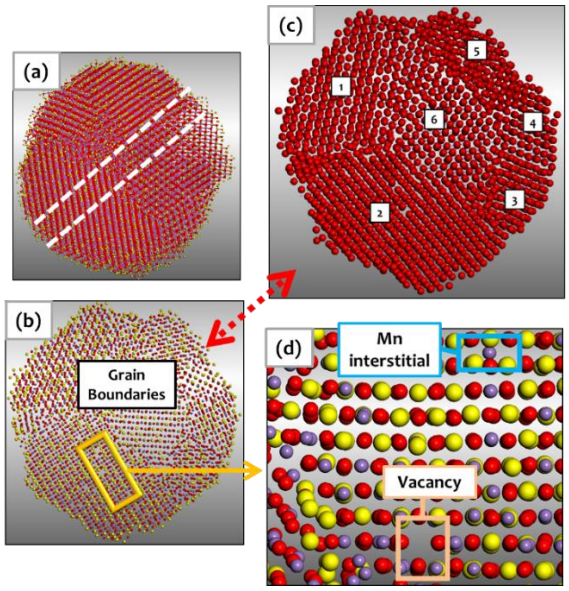

Figure 12: (a) Recrystallized $L_{1.75}Mn_2O_4$ nanosphere, (b) slice cut through nanosphere (c) grain boundary region and (d) point defects in the nanosphere.

X-ray Diffraction Patterns: Analysis of the model structures for mono-, intermediate and di-lithiated Li-Mn-O nanoparticles, with different lithium concentrations, have indicated the presence of co-existing spinel and layered domains. To further characterise the nanoparticles, calculated XRDs of the model systems are compared with experiments in fig 13. The diffraction pattern for simulated Li-Mn-O nanospheres with various concentrations is illustrated in figure 13 (a) and compared with (b) spinel $Li_4Mn_5O_{12}$ [29]**,** (c) spinel $LiMn_2O_4$ [30], (d) spinel $Li_2Mn_2O_4$ [30], (e) layered Li_2MnO_3 [30], (f) spinel Mn_3O_4 [31], (g) pure layered Li-Mn-O [9] and (h) layered/spinel Li-Mn-O **.** The first peak emerging on the diffraction patterns of the simulated nanospheres in (a), is a shoulder peak, around 2θ=20–25° which was identified as (020) and (110) peaks of monoclinic Li_2MnO_3 (C2/m). It is said to correspond with the ordering of Li and Mn atoms in the transition metal layers [9]. The simulated XRD has four other distinct peaks (2θ ~ 29, 39, 45 and 66 ^{0}). This growth of the [220] peak at 2θ ~ 29^0 is due to occupancy of a significant number of manganese ions in the tetrahedral sites of the spinel structure, forming Mn_3O_4 as a result of high temperature synthesis [32].

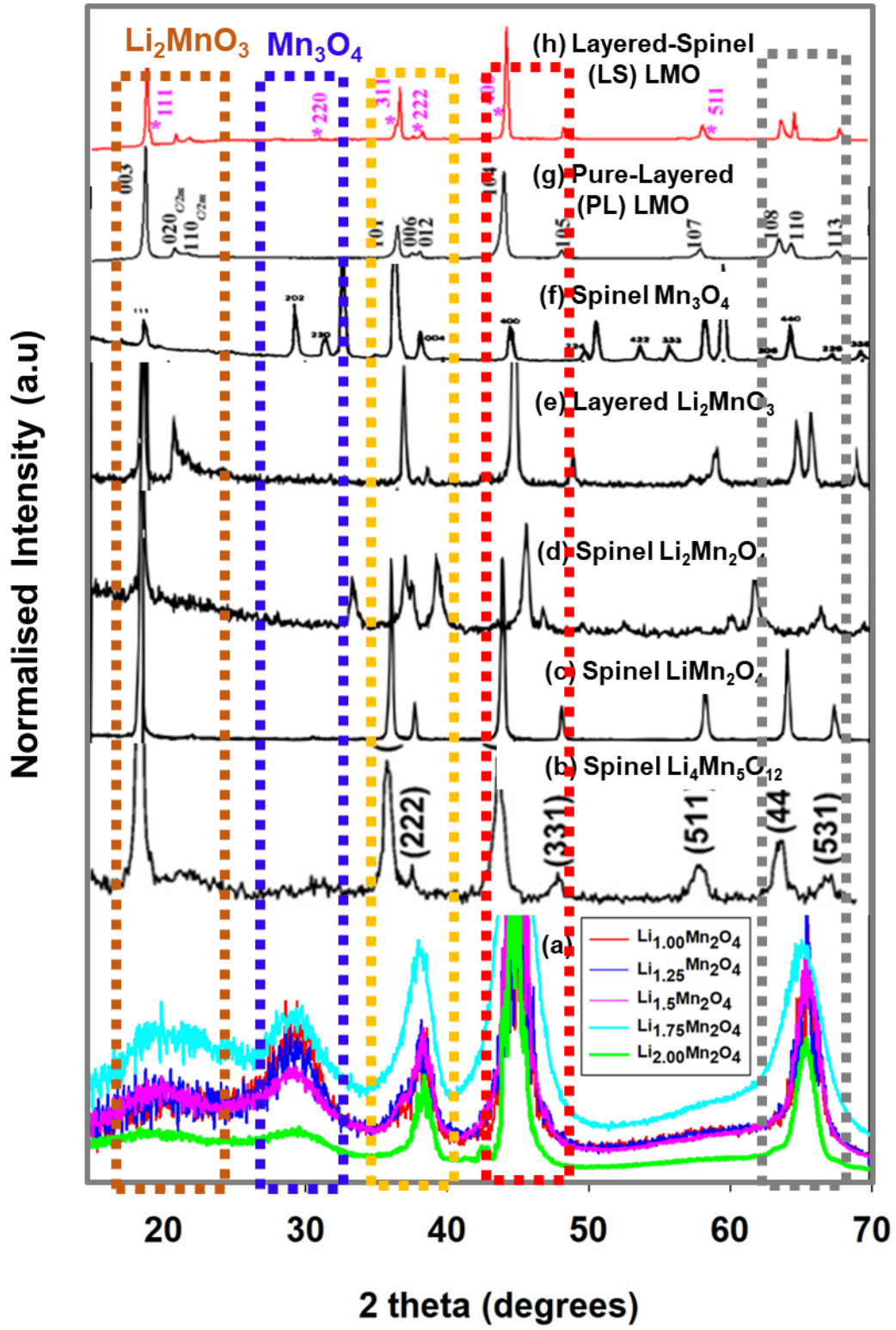

Figure 13: XRD patterns for (a) simulated layered/spinel nanospheres (this work), (b) spinel $Li_4Mn_5O_{12}$, [29] (c) spinel $LiMn_2O_4$ [30], (d) spinel $Li_2Mn_2O_4$ [30] (e) layered Li_2MnO_3 [30], (f) spinel Mn_3O_4 [31], (g) pure-layered Li-Mn-O [9] and (h) layered-spinel Li-Mn-O [9].

The third peak appears between 37^0 and 38^0 for all reference systems though not exactly at the same point as it seems to have shifted slightly towards 38 in other plots. This is followed by a very strong peak observed around 45^0 in the simulated diffraction pattern and corresponds to all reference XRDs from experiments. The last peak ($2\theta \sim 66^0$) appears to be a combination of peaks between 65 and 70 in the reference layered spinel and pure layered XRDs. Figure 14 represents diffraction plots for lithiated nanospheres ($Li_{1.00}Mn_2O_4$ $Li_{1.25}Mn_2O_4$, $Li_{1.5}Mn_2O_4$, $Li_{1.75}Mn_2O_4$ and $Li_{2.00}Mn_2O_4$) with magnified peaks in order to interrogate the effect of lithiation on the significant differences in peak intensity. The Li_2MnO_3 peak (Peak A) around 2θ = 20–25° has an almost constant peak intensity between $Li_{1.00}Mn_2O_4$ and $Li_{1.5}Mn_2O_4$. The peak then increases for the $Li_{1.75}Mn_2O_4$ nanosphere and flattens after complete lithiation at $Li_{2.00}Mn_2O_4$. Peak B at 2θ=29° (220) decreases with an increase in lithium

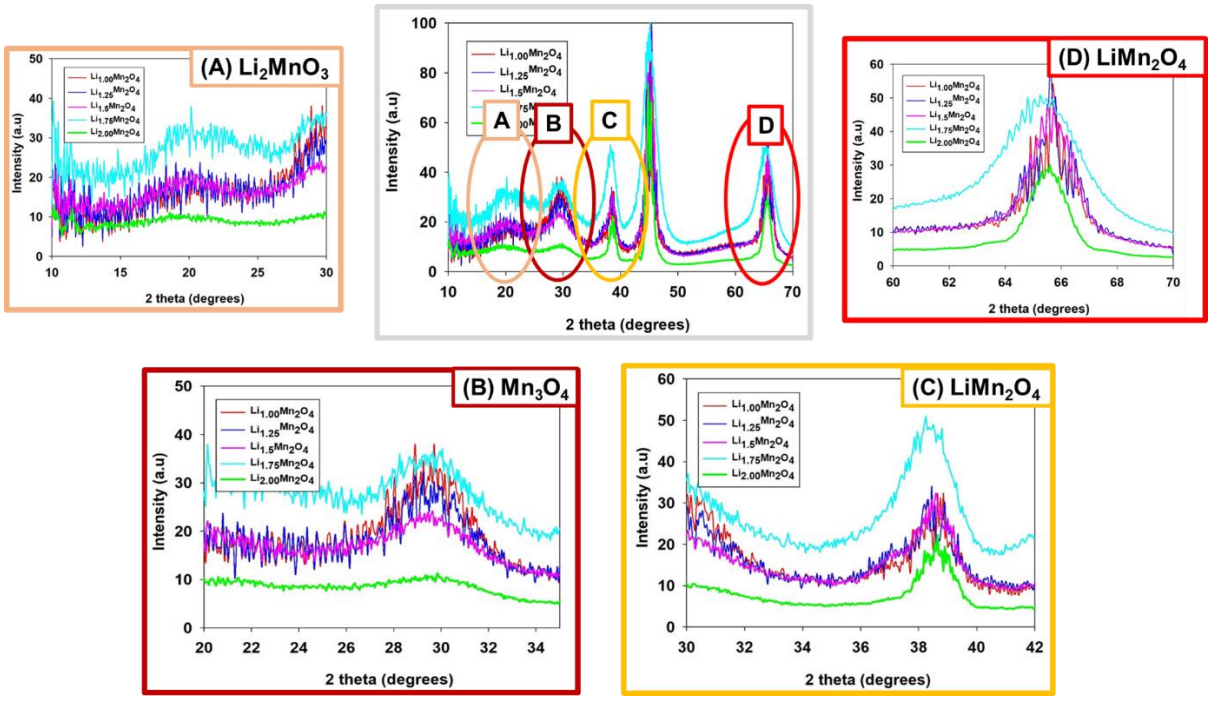

Figure 14: Superimposed X-Ray Diffraction (XRD) patterns of the simulated nanospherical models of: $LiMn_2O_4$ (red), $Li_{1.25}Mn_2O_4$ (royal blue), $Li_{1.5}Mn_2O_4$ (pink), $Li_{1.75}Mn_2O_4$ (cyan) and $Li_{2.00}Mn_2O_4$ (green). Magnification of the characteristic peaks for (A) Li_2MnO_3, (B) Mn_3O_4, (C) and (D) $LiMn_2O_4$.

concentration in the system, indicating reduction in tetragonally co-ordinated Mn^{2+} atoms and flattens drastically for the fully lithiated $Li_{2.00}Mn_2O_4$. Peak C emerges at

2θ~39, as a characteristic spinel peak and shift more towards $LiMn_2O_4$ (2θ~37.8^0) as the Li concentration increases in the nanosphere. The broad peak at 2θ~66^0 narrows with an increase in lithium concentration.

4. Discussions

Nucleation and growth of primary and secondary LMO and Li-rich manganese based NMC particles, with optimum tap density and well-rounded morphologies, is of great importance in providing good performance in Li-ion batteries; hence models that could contribute to these ideal properties are of essence. The current study has successfully synthesised $LiMn_2O_4$ nanoparticles, with an aid of crystalline seed, using simulated amorphization and recrystallization techniques. The amorphous nanoparticles were allowed to evolve, leading to crystallization, and a wide variety of structural features such as grain-boundaries and defects (interstitial, vacancies and substitutions), were captured within a single simulation cell. Such simulated particles are consistent with the widely reported cathode primary nanoparticles, which normally aggregate to form porous secondary particles [9, 33]. Furthermore, their dimensions (8nm) are within an order of magnitude of experimentally synthesised primary particles with diameters commencing from 20 nm. Simulated synthesis of larger systems and their aggregation, though computationally demanding, are currently underway and will provide valuable insights to the cracking and degradation of secondary particles during charging and discharging processes.

Another important aspect of the study is the generation of simulated composite or heterostructured cathode primary nanoparticles. Careful inspection of Li-Mn-O microstructural features, captured in structural snapshots and simulated XRDs, reveals that the nanoparticles crystallize into interconnected patterns with the presence of layered Li_2MnO_3-type and spinel domains, including $Li_4Mn_5O_{12}$ and Mn_3O_4. Such layered-spinel composites have been reported experimentally in Mn based ternaries [3]. In particular, surface post modification on Li-rich materials to form spinel membrane which encapsulated layered particles, has enhanced related rate capability and cycling stability [9, 11]. More significantly, layered layered composites of NMC, which yielded high specific capacity (~250 mAh/g), were partly corrected for voltage fade by controlled insertion of a spinel component [6] or by formation of platelets [7]

We now provide a rationale for the presence of several phases which are constituents of heterostructured nanoparticle, in the current study, where the amorphisation recrystallization method, which is a high temperature process, was applied on the spinel $LiMn_2O_4$. The occupancy of manganese atoms within some 3D tunnels of the recrystallized nanoparticles and lithium ions moving to the outer surface, instead of occupying 8a tetrahedral sites as expected in the pure spinel $LiMn_2O_4$, has been explained in a study by Thackeray al [32]. The formation of various high temperature structures, such as Li_2MnO_3 and Mn_3O_4, on heating the parent spinel $Li[Mn]_2O_4$ from ambient temperature, has been discussed in the introduction. In the current study, a mixture of seeds of such phases co-exist in the high temperature amorphous phase and leads to the formation of a heterostructure during the re-crystallisation of the nanoparticle, which is retained on annealing to 0K. On the contrary, a similar high temperature simulation study on a parent Li_2MnO_3 tends to yield nanoparticles without spinel components, since the layered phase is dominant both at low and high temperatures [23].

Related composites or heterostructures were previously synthesised by simulations for binary MnO_2 [20, 24] and TiO_2 [22, 34] nanoparticles, together with experimental syntheses of lithium manganese oxides [35, 36]. In contrast to previously simulated binaries, the complexity of the current $Li_xMn_2O_4$ heterostructured nanoparticle emanates from it being a ternary compound, compounded by the possibility of adopting several polymorphic crystal phases when synthesised at high temperatures. Here, we have captured such complexity by evolving the structures, starting from amorphous pre-cursors, rather than generating models using crystallographic symmetry operators. Consequently, the current study has paved a way for exploring performance optimisation of one of most promising cathodes, the Li-rich Mn based compound, by varying the content of its polymorphs.

We now consider how the simulated heterostructured nanoparticle is affected by lithiation, during discharge. The microstructural features deduced from crystallised nanoparticle are quite interesting. In the concentration range of $LiMn_2O_4$ to $Li_{1.50}Mn_2O_4$, large single crystalline and limited mulit-grained boundary regions are noted in each nanoparticle, and their location shifts with the Li content. However, at $Li_{1.75}Mn_2O_4$ the multigrained portion extends to the entire nanoparticle, which subsequently becomes single crystalline at $Li_2Mn_2O_4$ and depicts presence of the

tetragonal spinel phase. The microstructural images further show that whilst the lower Li concentration particles ($Li_{1.25}$ to $Li_{1.75}$) are clearly heterostructured, composed of the layered and spinel components, the one related to $Li_2Mn_2O_4$ is dominated by the spinel phase. Such features are consistent with the XRD patterns which are nearly superimposed in the range $Li_{1.0}$ to $Li_{1.50}$. However, distinct changes of XRD peaks are noted for the $Li_{1.75}Mn_2O_4$ concentration, where they are generally broadened. In case of the highest concentration, $Li_2Mn_2O_4$, the widths of the XRD peaks are suddenly reduced and significantly smaller than those of lower concentrations, $Li_{1.00}$ to $Li_{1.50}$. In addition, the peak height corresponding to the Li_2MnO_3 phase, at 2θ=20–25°, has been drastically reduced, together with that of the spinel Mn_3O_4 at 2θ=29° (220). The structural transition above $Li_{1.50}$ is somehow expected, since it is consistent with the reported marked reduction in voltage from 2.8 to 2.0V, depicted in Region III [ ]. This is accompanied by a symmetry change from cubic spinel Fd-3m to tetragonal spinel $I4_1/amd$, where the occupation of 8a sites by Li is minimal and that of 16c is prevalent [30]**,** which is clearly depicted in our simulated microstructures. Whilst previous work has extensively discussed structures and phenomena occurring at $Li_{1.50}$ and $Li_{2.0}$, the current study has explicitly highlighted the emergence, presence and disappearance of an intermediate phase $Li_{1.75}Mn_2O_4$,

In the study of thermal stability for spinel, the Li_2MnO_3-layered structure emerged as a result of lithium and oxygen loss to the surface thus later forming Mn_3O_4 at high temperatures. The study indicated internal redox reaction was responsible for generating a defected spinel phase in which Mn^{2+} (d^5) ions are stabilized in tetrahedral (8a) coordination in Mn_3O_4 as this is a high temperature spinel phase [37]. However, when surplus lithiums were intercalated into the nanoparticles, the concentration of Mn^{2+} atoms in tetrahedral sites was reduced as evident in the microstructures (figure 9) and XRD patterns (figure 14, where the [211] peak at 2θ=29° decreased with increasing lithium concentration. This is in line with the prediction that 16c octahedral sites are more favourable than tetrahedral sites during cycling owing to less energy being required to remove lithium ions from the octahedral sites than the tetrahedral sites of the $Li[Mn_2]O_4$ spinel. The XRD patterns also showed an increase in lithium concentration constituted to the formation of more spinel $LiMn_2O_4$ type structure within the nanoparticle.

The impact of layered components within the spinel-structured nanoparticles needs to be well understood to clarify the effect of its existence within the electrode material and how it would affect the electrochemical performance of the material. Several studies have been carried out in the past on the Li_2MnO_3 cathode in lithium cells, either in isolation or as a component in layered–spinel composite electrodes (M = Mn, Ni) in which the layered Li_2MnO_3 and $LiMO_2$ component oxide materials are structurally integrated, via a shared common oxygen sub-lattice, at the atomic level. Findings from the work of Johnson et al [3] during the investigation of electrochemical performance of spinel-layered composites indicated that Li_2O could be partially extracted from the Li_2MnO_3 component, whilst retaining an electrochemically active layered MnO_2 component in which lithium can be inserted and extracted. These findings advised that the layered-spinel composite electrodes are technologically important because of their high voltage (>4.5V) and high storage capacity (>250 mAh/g). Accordingly, the layered spinel component is important in achieving both high storage capacities and (three-dimensional) lithium transport pathways.

Our findings epitomise the need to have models, which capture the structural complexity of the real material. This includes: the atomistic structure and connectivity of the network of pores, the exit holes through which the Li ions intercalate and deintercalate from the material and the microstructure of the material (microtwinning and connectivity of the 1 x 1 tunnels, (point) defects, dislocations and more general grain-boundaries). Moreover, to simulate the diffusion process, where the mobility of Li is likely concerted, a high number of Li ions must be included within a single simulation cell to capture the diverse range of correlated mechanisms associated with Li mobility. At present, the number of atoms required to capture all these features within a single model is too large to be considered quantum mechanically (using for example, density functional theory) and therefore atomistic simulation, using pair potentials, continues to provide a valuable tool to be used in conjunction with quantum mechanical methods; together they provide unique insight for experiment.

5. Conclusion

Atom-level models, for Li-Mn-O composite/heterostructured nanoparticles, were synthesised by simulating the crystallisation of the system, starting from amorphous precursors. The presence of the layered (Li_2MnO_3) and spinel (Mn_3O_4, $LiMn_2O_4$,

$Li_4Mn_5O_{12}$) polymorphs were deduced from microstructural features and XRD patterns. The discharge of the nanoparticle by lithiation, in the range $LiMn_2O_4$ to $Li_{1.5}Mn_2O_4$ does not reflected much change in structure since it all corresponds to the cubic Fd-3m spinel. However, a significant change to a multigrained structure is noted at the intermediate phase, $Li_{1.75}Mn_2O_4$, which is confirmed by visualised nanoparticles and substantially broadened XRDs. Upon further discharge, a transition to a tetragonal spinel, with the symmetry $I4_1/amd$, is noted at $Li_2Mn_2O_4$ and the spinel phase appears to be dominant at such highest concentration. Contrary to most previous work, such deductions are drawn from a technique (simulated amorphisation recrystallization) that allows spontaneous generation of large nanoparticles (26 000 atoms) at various Li concentrations.

Specifically, we show how the layered components and microstructural features, are important in achieving both high storage capacities and (three-dimensional) lithium transport pathways. The microtwinning enables channels (for Li mobility) to traverse all three spatial directions. The Li_2MnO_3 component allows for extraction of Li_2O enabling charge cycling whilst retaining an (electrochemically active) MnO_2 layer. The intrinsic defects, including vacancies and substitutionals help facilitate mobility of Li through the lattice during charge cycling by providing additional pathways and increase three-dimensional connectivity of the pathways so that Li can move freely throughout the material.

Acknowledgements

We acknowledge support of the South African Research Chair Initiative of the Department of Science and Technology and the National Research Foundation in Pretoria and the Centre for High Performance Computing in Cape Town.

References for previous draft.

References

[1] Fu F., Xu G. L., Wang Q., Deng Y. P., Li X., Li J. T., Huang L. and Sun S. G., "Synthesis of Single Crystalline Hexagonal Nanobricks Of $LiNi_{1/3}Co_{1/3}Mn_{1/3}O_2$ With High Percentage of Exposed {010} Active Facets as High Rate Performance Cathode Material for Lithium-Ion Battery," *Journal of Materials Chemistry A,* **1**, 3860-3864, 2013

[2] Thackeray M. M., Wolverton C. and Isaacs E. D., "Electrical Energy Storage For Transportation—Approaching The Limits of, and Going Beyond, Lithium-Ion Batteries," *Energy & Environmental Science,* **5**, 7854-7863, 2012

[3] Johnson C. S., Li N., Vaughey J. T. , Hackney S. A. and Thackeray M. M., "Lithium–Manganese Oxide Electrodes with Layered–Spinel Composite Structures $xLi_2MnO_3 \cdot (1-x)\ Li_{1+y}Mn_{2-y}O_4$ ($0< x< 1$, $0 \leqslant y \leqslant 0.33$) for Lithium Batteries," *Electrochemistry Communications,* **7**, 528-536, 2005

[4] Yang C., Zhang Q., Ding W., Zang J., Lei M., Zheng M. and Dong Q., "Improving The Electrochemical Performance of Layered Lithium-Rich Cathode Materials by Fabricating a Spinel Outer Layer With Ni^{3+}," *Journal of Materials Chemistry A,* **3**, 7554-7559, 2015

[5] Gu M., Belharouak I., Zheng J., Wu H., Xiao J., Genc A., Amine K., Thevuthasan S., Baer D. R., Zhang J. G. and Browning N. D., "Formation of the Spinel Phase in the Layered Composite Cathode Used in Li-ion Batteries," *ACS Nano,* **7**, 760-767, 2012

[6] Long B. R., Croy J. R., Park J. S., Wen J., Miller D. J. and Thackeray M. M., "Advances In Stabilizing 'Layered-Layered'$xLi_2MnO_3 \cdot (1-X)\ LiMO_2$ (M= Mn, Ni, Co) Electrodes With A Spinel Component," *Journal Of The Electrochemical Society,* **161**, A2160-A2167, 2014

[7] Wang D., Belharouak I., Zhou G. and Amine K., "Nanoarchitecture Multi-Structural Cathode Materials for High Capacity Lithium Batteries," *Advanced Functional Materials,* **23**, 1070-1075, 2013

[8] Lim J. M., Hwang T., Kim D., Park M. S., Cho K. and Cho M., "Intrinsic Origins Of Crack Generation in Ni-Rich $LiNi_{0.8}Co_{0.1}Mn_{0.1}O_2$ Layered Oxide Cathode Material," *Scientific Reports,* **7**, 39669 - 39669, 2017

[9] Deng Y. P., Yin Z. W., Wu Z. G., Zhang S. J., Fu F., Zhang T., Li J. T., Huang L. and Sun S.G., "Layered/Spinel Heterostructured and Hierarchical Micro/Nanostructured Li-Rich Cathode Materials With Enhanced Electrochemical Properties For Li-Ion Batteries," *ACS Applied Materials & Interfaces,* **9**, 21065-21070, 2017

[10] Luo D., Li G., Fu C., Zheng J., Fan J., Li Q. and Li L., "A New Spinel-Layered Li-Rich Microsphere As A High-Rate Cathode Material For Li-Ion Batteries," *Advanced Energy Materials,* **4**, 1400062-1400062, 2014

[11] Deng Y. P., Fu F., Wu Z. G., Yin Z. W., Zhang T., Li J. T., Huang L. And Sun S. G., "Layered/Spinel Heterostructured Li-Rich Materials Synthesized By A One-Step Solvothermal Strategy With Enhanced Electrochemical Performance For Li-Ion Batteries," *Journal of Materials Chemistry A,* **4**, 257-263, 2016

[12] Wu F., Li N., Su Y., Shou H., Bao L., Yang W., Zhang L., An R. and Chen S., *Advanced Materials,* **25**, 3722-3726, 2013

[13] Huang H., Vincent C. A. and Bruce P. G, "Correlating Capacity Loss of Stoichiometric and Nonstoichiometric Lithium Manganese Oxide Spinel Electrodes With Their Structural Integrity," *Journal of the Electrochemical Society,* **146**, 3649-3654, 1999

[14] Xia H., Luob Z. and Xieb J., "Nanostructured $LiMn_2O_4$ and Their Composites as High-Performance Cathodes for Lithium-Ion Batteries," *Progress In Natural Science: Materials International,* **22**, 572-584, 2012

[15] Wang S., Wu Y., Li Y., Zheng J., Yang J., And Yang Y., "Li $[Li_{0.2}Mn_{0.54}Ni_{0.13}Co_{0.13}]O_2$–$LiMn_{1.5}Ti_{0.5}O_4$ Composite Cathodes With Improved Electrochemical Performance For Lithium Ion Batteries," *Electrochimica Acta,* **133**, 100-106, 2014

[16] Jeong S. K., Shin J. S., Nahm K. S., Kumar T. P. and Stephan A. M, "Electrochemical Studies on Cathode Blends Of $LiMn_2O_4$ and Li $[Li_{1/15}Ni_{1/5}Co_{2/5}Mn_{1/3}O_2]$," *Materials Chemistry and Physics,* **111**, 213-217, 2008

[17] Sun Y. K., Lee M. J., Yoon C. S., Hassoun J., Amine K. and Scrosati B., "The Role Of AlF_3 Coatings in Improving Electrochemical Cycling of Li-Enriched

Nickel-Manganese Oxide Electrodes For Li-Ion Batteries," *Advanced Materials,* **24**, 1192-1196, 2012

[18] Zheng J., Gu M., Xiao J., Polzin B. J., Yan P., Chen X., Wang C. and Zhang J. G., "Functioning Mechanism Of AlF_3 Coating on the Li- and Mn-Rich Cathode Materials," *Chemistry of Materials,* **26**, 6320-6327, 2014

[19] Wang D., Yu R., Wang X., Ge L. and Yang X., "Dependence of Structure and Temperature for Lithium-Rich Layered-Spinel Microspheres Cathode Material of Lithium Ion Batteries," *Scientific Reports,* **5**, 8403-8403, 2015

[20] Sayle T. X. T., Catlow C. R. A., Maphanga R. R., Ngoepe P. E. and Sayle D. C., "Generating MnO_2 Nanoparticles Using Simulated Amorphization and Recrystallization," *Journal of the American Chemical Society,* **127**, 12828-12837, 2005

[21] Sayle T. X. T., Maphanga R. R., Ngoepe P. E. And Sayle D. C., "Predicting The Electrochemical Properties of MnO_2 Nanomaterials Used In Rechargeable Li Batteries: Simulating Nanostructure at the Atomistic Level," *Journal of the American Chemical Society,* **131**, 6161-6173, 2009

[22] Sayle D. C. and Sayle T. X. T., "High-Pressure Crystallisation of TiO_2 Nanoparticles," *Journal of Computational And Theoretical Nanoscience,* **4**, 299-308, 2007

[23] Sayle T. X. T., Caddeo F., Monama N. O., Kgatwane K. M., Ngoepe P. E. and Sayle D. C., "Origin Of Electrochemical Activity In Nano-Li_2MnO_3; Stabilization via a 'Point Defect Scaffold'," *Nanoscale,* **7**, 1167-1180, 2015

[24] Maphanga R. R., Sayle T. X. T., Ngoepe P. E. and Sayle D. C., "Amorphization and Recrystallization Study of Lithium Insertion Into Manganese Dioxide," *Physical Chemistry Chemical Physics,* **13**, 1307-1313, 2011

[25] Liu C., Neale Z. G. and Cao G., "Understanding Electrochemical Potentials of Cathode Materials In Rechargeable Batteries," *Materials Today,* **19**, 109-123, 2016

[26] Ledwaba R. S., Matshaba M. G. And Ngoepe P. E., "Molecular Dynamics Simulations of Spinels: $LiMn_2O_4$ and $Li_4Mn_5O_{12}$ at High Temperatures," In *IOP*

Conference Series: Materials Science And Engineering, Canterbury, **80**, 012024, 2015

[27] Smith W. and Forester T. R., "DL_POLY_2. 0: A General-Purpose Parallel Molecular Dynamics Simulation Package," *Journal of Molecular Graphics,* **14**, 136, 1996

[28] Park S. H., Myung S. T., Oh S. W., Yoon C. S. and Sun Y. K., "Ultrasonic Spray Pyrolysis of Nano Crystalline Spinel $LiMn_2O_4$ Showing Good Cycling Performance in the 3 V Range," *Electrochimica Acta,* **51**, 4089-4095, 2006

[29] Song B., Veith G. M., Park J., Yoon M., Whitfield P. S., Kirkham M. J., Liu J. and Huq A., "Metastable $Li_{1+\delta}Mn_2O_4$ ($0 \leq \delta \leq 1$) Spinel Phases Revealed by in Operando Neutron Diffraction and First-Principles Calculations," *Chemistry of Materials,* **31**, 124-134, 2018

[30] Hao Y. J., Lai Q. Y., Xu X. Y. and Wang L., "Electrochemical Performance of Symmetric Supercapacitor Based on $Li_4Mn_5O_{12}$ Electrode in Li_2SO_4 Electrolyte," *Materials Chemistry and Physics,* **126**, 432-432, 2011

[31] Choa J. and Thackeray M. M., "Structural Changes of $LiMn_2O_4$ Spinel Electrodes During Electrochemical Cycling," *Journal of the Electrochemical Society,* **146**, 3577-3581, 1999

[32] Thackeray M. M., David W. I. F., Bruce P. G. and Goodenough J. B., "Lithium Insertion Into Manganese Spinels," *Materials Research Bulletin,* **18**, 461-472, 1983

[33] Thackeray M. M., Mansuetto M. F., Dees D. W. and Vissers D. R., "The Thermal Stability of Lithium-Manganese-Oxide Spinel Phases," *Materials Research Bulletin,* **31**, 133-140, 1996

[34] Gilbert J. A., Bareño J., Spila T., Trask S. E., Miller D. J., Polzin B. J., Jansen A. N. and Abraham D. P., "Cycling Behavior Of NCM523/Graphite Lithium-Ion Cells in the 3–4.4 V Range: Diagnostic Studies Of Full Cells And Harvested Electrodes," *Journal of the Electrochemical Society,* **164**, A6054-A6065, 2017

[35] Matshaba M. G., Sayle D. C., Sayle T. X. and Ngoepe P. E., "Structure of Surface Entrance Sites For Li Intercalation Into Tio2 Nanoparticles, Nanosheets and Mesoporous Architectures With Application for Li-Ion Batteries," *The Journal of Physical Chemistry C,* **120**, 14001–14008, 2016

[36] Johnson C. S., Mansuetto M. F., Thackeray M. M., Shao-Horn Y. and Hackney S. A., "Stabilized Alpha-Mno2 Electrodes For Rechargeable 3 V Lithium Batteries," *Journal of The Electrochemical Society,* **144**, 2279-2283, 1997

[37] Komaba S., Sasaki T. and Kumagai N., "Preparation And Electrochemical Performance of Composite Oxide of Alpha Manganese Dioxide and Li–Mn–O Spinel," *Electrochimica Acta,* **50**, 2297-2305, 2005

[38] Thackeray M. M., "Manganese Oxides For Lithium Batteries," *Progress In Solid State Chemistry,* **25**, 1-71, 1997